

# Computational Analysis of Three-Dimensional Turbulent Viscous/Inviscid Interactions

Datta V. Gaitonde

*Air Vehicles Directorate*

*Air Force Research Laboratory*

*Wright-Patterson Air Force Base, Ohio, USA*

*Email: datta@vaa.wpafb.af.mil*

## Abstract

Numerical simulations with the full mean compressible Navier–Stokes equations, supplemented with several turbulence models, are utilized to comprehend the complex three-dimensional events accompanying the interaction of swept shock-waves with turbulent boundary layers. Both internal and external situations are analyzed with the double-fin and cylinder/offset-flare as prototypes. The flow parameters together span a wide range of Mach and Reynolds numbers. A unified understanding is derived by examining flow features whose fidelity can be established by comparison with experimental data. Particular emphasis is placed on deducing and characterizing the resultant flowfields in terms of simple coherent regimes. These descriptions are then employed to comment briefly on the problem of turbulence modeling for such flows.

## 1 Introduction

The recent resurgence of interest in the development of vehicles capable of sustained hypersonic flight has invigorated efforts to investigate phenomena occurring in such environments. The interaction of shock

waves with turbulent boundary layers constitutes one such class of events. If the shock is of sufficient strength, the consequences include three-dimensional separation and the formation of vortical structures. The concomitant reduction in pressure recovery and increase in distortion degrade performance of aircraft components and limit vehicle operational envelopes. A clear understanding of the fundamental physics is a critical component of efforts to improve systems designed to operate at very high speeds.

Over the past two decades, advances in numerical algorithms and turbulence modeling, supplemented with rapid increases in computational speed, have provided great impetus to the numerical simulation and understanding of three-dimensional shock-wave/turbulent boundary layer interactions (STBLI). High-resolution upwind methods have made the precise capture of shocks a routine matter. Success has been more limited in the development of more accurate turbulence models. Although specialized turbulence models have been proposed to compute various types of flowfields, a universal treatment remains elusive.

Basic studies of STBLI are generally performed in geometrically simple configurations in which the pertinent fluid dynamic mechanisms can be isolated. Typically, shock generators are mounted on a surface, such as a plate or cylindrical body, which provides a platform for the turbulent boundary layer. Research groups in several countries have been active and insightful contributors in these studies. The present article does not purport to provide a survey of these efforts: the reviews of Settles and Dolling [1], Panaras [2], and Zheltovodov [3] should be consulted for this purpose.

This article, based on recent efforts of the author and his colleagues, is focused primarily on describing the manner in which computations may be utilized to develop simple but unified descriptions of STBLI. Two examples are chosen to illustrate these procedures: the double-fin (Figure 1 (top)) and the cylinder/offset flare (Figure 1 (bottom)), representing internal and external interactions, respectively. The principal flow parameters determining the features of the interaction include the Mach and Reynolds numbers, the properties

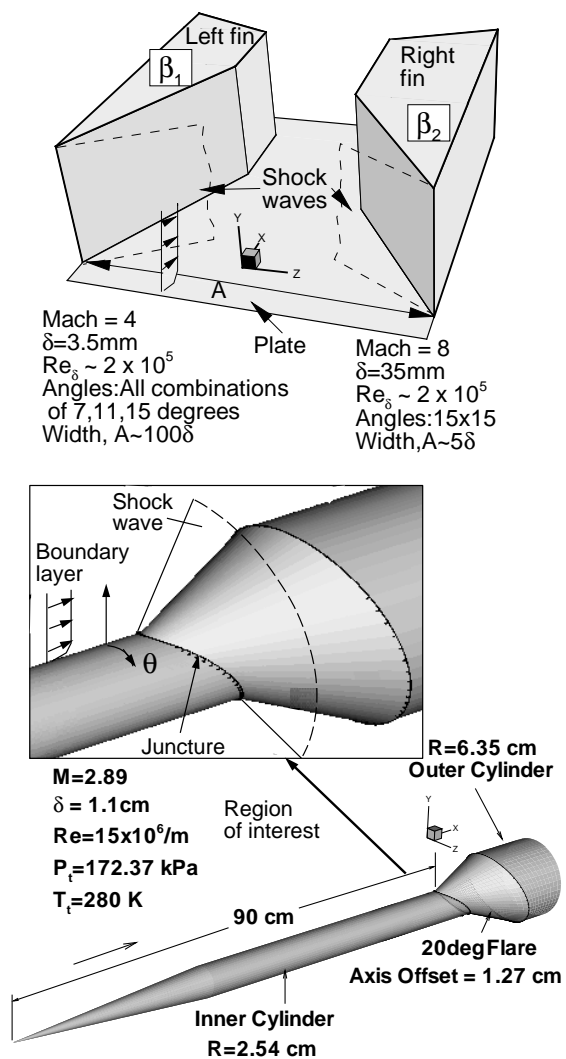


Figure 1: Three-dimensional configurations examined. Top: crossing-shock (double-fin); bottom: cylinder/offset-flare.

of the incoming boundary layer, the wedge angles determining shock strength and the wall thermal conditions. Some of these parameters are marked in Figure 1. Of the two configurations, the double-fin is by far the more extensively investigated and a range of parameters is considered for this situation. In contrast, the analysis of the cylinder/offset flare flowfield is performed with a single set of data.

Since numerical simulations are a major component of the present study, it is important to judge their fidelity to the physics. Experimental investigations play a critical role by providing a framework for validation. Indeed, the parameters listed in Figure 1 were chosen after careful consideration of experimental data derived from several sources [4–8]. The numerical simulations employed here have been appraised in [9–12] and clearly identify those aspects of STBLI amenable to further exploration with the present computational approaches. These studies conclude that dominant aspects of the computed mean flowfield structure are relatively insensitive to the turbulence model. Further, all large-scale features are in excellent agreement with experimental data. References [9, 12] demonstrate this for the double-fin by reproducing experimental surface pressure, pitot pressure surveys, surface oil flow and shock structure. For the cylinder/flare interaction, favorable comparisons of upstream influence, surface oil flow and surface pressure have been published in [10, 11].

The literature also reveals two primary deficiencies of computational techniques. First, these do not reproduce the inherent unsteadiness in such flows: a discussion of the pertinent issues may be found in [1, 13]. The results described in the present effort are therefore relevant to those aspects of the computed *mean* flow structure whose fidelity has been well established. Second, quantitative values of heat transfer rates and skin-friction coefficients are poorly estimated [14–16]. Unlike for the large-scale features, these quantities are strongly dependent on the turbulence model, which is the major source of inaccuracy. Indeed, it will be proven shortly that the flow structure is highly three-dimensional. Turbulent mechanisms in 3D situations can be fundamentally different from and without analog in 2D (e.g., [17]). Thus, it should come as no great surprise that

common compressible turbulence models, which are generally direct extensions of their 2D counterparts, fail in certain respects. This paper will conclude by leveraging an understanding of the flow structure to clarify these computational deficiencies and to comment on turbulence modeling.

## 2 Theoretical model

The flow structure is deduced by computing solutions to the full 3D mean compressible Navier–Stokes equations written in strong conservation form and mass-averaged variables [18]. A perfect gas with a Prandtl number of 0.72 is assumed and the molecular viscosity is obtained from Sutherland’s law. The effects of turbulence are incorporated through the eddy viscosity,  $\mu_t$ , assumption and the turbulent Prandtl number is taken to be 0.9. A specification of the numerical method requires detailing of the differencing scheme as well as of the turbulence model. The results described here are based on a large number of calculations in which the treatment of each of these two components varies widely. While the viscous terms are invariably centrally differenced, both finite-difference centered and finite-volume upwind schemes have been assessed for the inviscid terms. For the crossing-shock configuration, the algebraic Baldwin-Lomax [19] and several variants of the popular two-equation  $k$ - $\epsilon$  model [20] have been evaluated, while for the cylinder/offset-flare case, the one-equation models of [21,22] were also considered. The interested reader may find implementation details in [23,24]. These specifics are not belabored here because, as noted earlier, the major aspects of interest in this study are predicted equally well with each of the numerical models employed. Further comment on this rather surprising result is reserved for later.

An adequate computational mesh is crucial towards ensuring accuracy. The present configurations are simple enough that generating a suitable mesh is not a difficult task. For the double-fin, non-uniform Cartesian planes are stacked sequentially in the stream-wise direction. Sufficient resolution is ensured by clustering mesh points near

solid surfaces and to a lesser extent near the central region of the channel formed by the two fins. Based on a number of resolution studies [9,14], the mesh employed consists of  $123 \times 88 \times 197$  points in the stream-wise, plate-normal and span-wise directions, respectively. For symmetric cases, only one half of the domain is computed and the number of span-wise points is halved. For the cylinder/offset-flare configuration, a radial mesh clustered near the surface is more effective, and adequate resolution is afforded with a mesh of  $113 \times 125 \times 115$  points [11].

Each of the above meshes spans only the interaction region, which extends a few boundary layer thicknesses upstream of the shock generator. At this upstream location, the boundary layer profile is specified to match experimental data – momentum thickness for the double-fin and skin-friction coefficient for the cylinder-flare. These profiles are generated with separate 2D or axi-symmetric codes to reduce the computational requirement. The other boundary conditions are enforced in a straightforward manner. On all solid surfaces, there is no slip, the wall temperature is set to the experimentally reported value and the normal pressure gradient is zero from the boundary layer approximation. Similarly, zero gradient is assumed for all flow quantities at the downstream and far field boundaries.

### 3 Streamline structure

#### 3.1 Crossing shock interaction

One of the most common observations obtained from experiment is of the surface oil flow pattern on the plate. The numerical equivalent to such traces is generated by releasing computational particles at the first mesh point away from the plate and zeroing the normal component of velocity. The computed result obtained with the  $k-\epsilon$  turbulence model for the Mach 4,  $15 \times 15$  case, i.e. where  $\beta_1 = \beta_2 = 15$  deg in Figure 1, is shown in Figure 2 (top). The experimentally inferred pattern, taken from [4], is reproduced in Figure 2 (bottom). A sketch is utilized rather than the actual film because the latter does

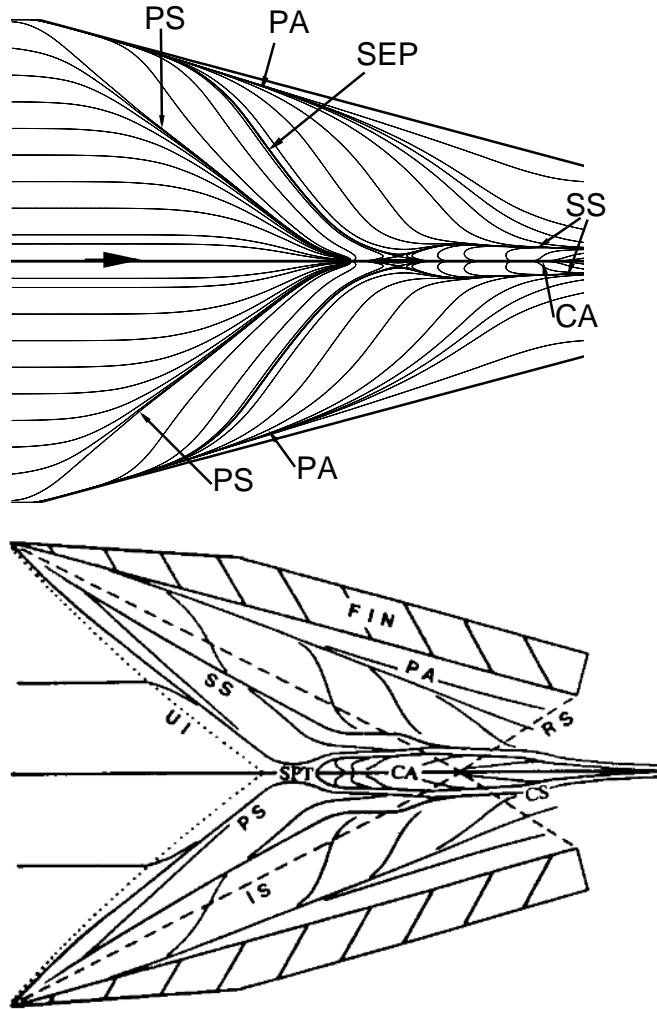


Figure 2: Surface streamline patterns in  $15 \times 15$  Mach 4 configuration. Top: computed result with the  $k-\epsilon$  model; bottom: experimental inference of [4], reproduced with permission. Not to same scale.

not reproduce well electronically.

Each pattern depicts several asymptotic lines on which “surface streamlines” appear to coalesce, and others from which they appear to diverge. These features are typically associated with separation and attachment respectively — [25,26] contain a detailed discussion of the significance of these portraits. Referring to Figure 2(top), the two lines of coalescence which form in the upstream region are denoted PS for primary separation while those that form downstream, parallel to and straddling the line of symmetry, are denoted SS for secondary separation. Similarly, the two lines of divergence forming symmetrically near the fin-plate juncture are termed PA for primary attachment and the line of attachment on the centerline is denoted CA. It is evident that each of these dominant features is reproduced fairly accurately by the computations. A separatrix, SEP, whose significance will be clarified shortly, is also marked in the numerical result. Each of these features is also observed in the experimental inference (Figure 2(bottom)). The discrepancies may be characterized primarily as differences in interpretation — for example, the upstream segment of SS in the experimental inference more closely corresponds to the separatrix in the computation. A similar arrangement of principal surface streamlines has been observed at higher Mach numbers [14,27].

As an example of an asymmetric case, Figure 3, displays computed results (top), again with the  $k-\epsilon$  model, with the inferred sketch of Zheltovodov et al. [8] for the Mach 4,  $7 \times 15$  case. The notation followed in this figure differs from that of Figure 3 for chronological reasons. The three cross-flow lines marked I, II, and III in the experimental sketch are locations where surface measurements are available, as discussed later. It is apparent that the agreement between computation and experiment continues to be very good even when the interactions caused by the two fins differ substantially in strength. For clarity, the upstream influence line,  $U$ , is not marked in the computation though it can easily be identified at the initial location of turning of the surface streamlines. The two primary lines of coalescence are denoted  $S_1$  and  $S_2$ . The former is much weaker



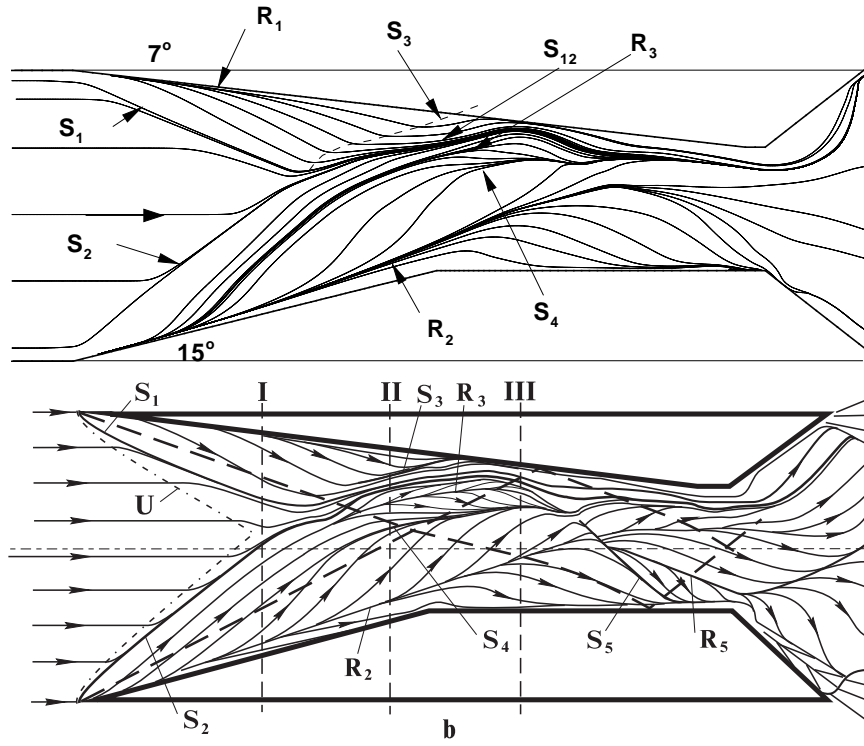


Figure 3: Surface streamline patterns in Mach 4,  $7 \times 15$  configuration. Top: computed result with the  $k-\epsilon$  model; bottom: experimental inference of Zheltovodov et al. [8], reproduced with permission. Not to same scale.

than the latter because of the milder nature of the 7 degree interaction. As they approach each other near the centerline,  $S_1$  and  $S_2$  gradually lose their independent identities. The combined downstream segment, denoted  $S_{12}$  in the simulation, approaches the 7 degree fin before turning back toward the center of the channel. Between  $S_{12}$  and the 15 degree fin, a line of divergence,  $R_3$ , and one of coalescence,  $S_4$ , are clearly evident. The pocket between  $S_{12}$  and  $S_4$  collapses rather abruptly. Beyond this point, the flow turning angles are similar in computation and experiment.

A close scrutiny of the symmetric and asymmetric patterns permits a clear topological association to be made between the two. Specifically,  $S_1$  and  $S_2$  (Figure 3) may be considered as direct counterparts of the two PS segments (Figure 2), while  $R_1$  and  $R_2$  bear a similar relationship to the two PA segments. The analogy is completed by linking  $S_{12}$  and  $S_4$  with the two SS segments on either side of the line of symmetry and  $R_3$  with CA.

The surface oil flow pattern bears a close relationship to the various coherent regimes in the flowfield which are more difficult to visualize experimentally. Indeed, the surface patterns are often viewed as “footprints” of the flowfield and several efforts have successfully established broad guidelines to construct the 3D flowfield from surface patterns [25, 26, 28]. However, the relationship between surface and off-surface fluid behavior is not unique – [29] contains an illuminating example which emphasizes the need for caution when constructing flowfield models based solely on surface oil patterns.

Although computational results contain all the information required to construct a particle-path-based three-dimensional model, the task of extracting a simple description can be overwhelming if particles are released without judicious choice. In the present case, we employ the fact that lines of coalescence are associated with three-dimensional dividing surfaces which distinguish various regimes [26]. Therefore, a simple stratagem is to release particles on either side of such lines and to trace their trajectories in time, both forwards and backwards. This latter action is meaningful in a (mean) steady flowfield. The different particle traces are then joined to form ribbons

which facilitate an elegant description of the flowfield.

The results of following the above procedure are shown in Figure 4 for the Mach 4,  $15 \times 15$  case. For clarity, an artificial aspect ratio has been applied. This result was obtained with the  $k-\epsilon$  model, though, as noted earlier, the same regimes can be extracted with any of the other models examined. The features of the computed flowfield can be summarized as follows:

- Separated boundary layer (BL): The upstream boundary layer separates from the plate at the primary line of separation, PS. This fluid does not reattach to the plate. The interaction channels particles from near the fins towards the center where the profile of the separation surface changes to an arch-like form.

Fluid attaching at PA can be distinguished into two regimes:

- Vortex interaction regime (VI): Fluid attaching at the segment of PA between PS and SEP sweeps span-wise and separates from the downstream side of PS to form a shear layer with the separated boundary layer. This regime manifests off-surface stagnation points on the symmetry-plane as described later.
- Entrainment flow (EF): High-speed fluid attaching at PA downstream of SEP sweeps across the channel and separates prior to reaching the centerline from the fin-side of SS.
- Secondary vortex (SV): Some fluid, also originating near the fin leading edges, is swept span-wise towards the symmetry plane and is subsequently turned stream-wise. This fluid attaches at CA and separates from the symmetry plane side of SS to form two mirror counterparts of a secondary vortex.

A primary vortical structure, considered as coherent helical motion about a three-dimensional axis, can be constructed from a combination of the BL, VI, and EF regimes.

The analogy established between the symmetric and asymmetric “footprints” permits a straightforward extension of the above flowfield model to asymmetric interactions. The same four regimes can

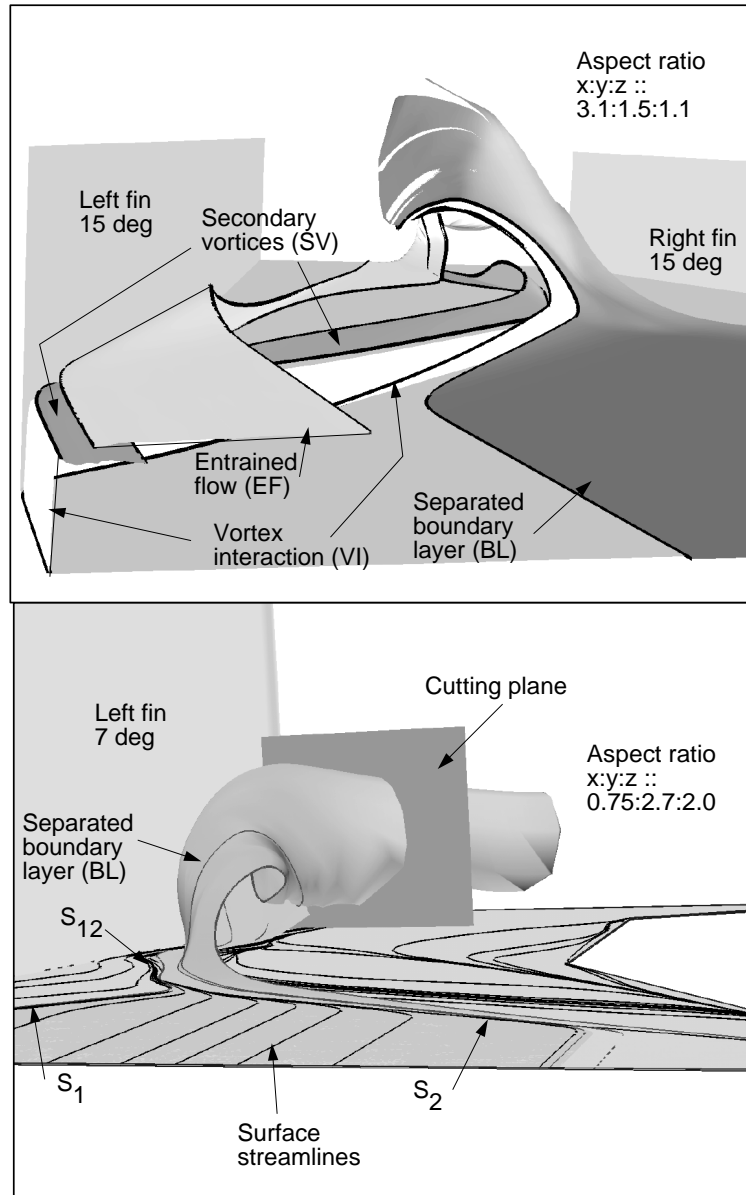


Figure 4: Flow structure at Mach 4 with ribbons. Top:  $15 \times 15$ . Bottom:  $7 \times 15$ .

be identified, though the form of each is distorted from that observed in the symmetric interaction. For example, the surface formed by the separated boundary layer is shown in Figure 4(bottom) for the  $7 \times 15$  interaction together with some surface oil flow lines to provide points of reference. On the strong (15 degree) interaction side, the surface rises rapidly in the vicinity of  $S_2$  with particles sweeping span-wise towards the 7 degree fin. The subsequent roll-up to form a vortical structure is clearly evident. On the weak interaction side, the particles initially exhibit relatively little movement away from the surface but separate rapidly downstream. A consequence of the asymmetry is that the primary vortical structure impinges on the 7 degree sidewall. The complicated events accompanying this process are investigated further in a later section. Detailed figures of the other regimes in an asymmetric interaction may be found in [12].

The above description has proved to be applicable for a wide range of parameters. The same four structures have been detected in all cases where the incoming boundary layer separates from the plate (strong interactions). These include the Mach 8,  $15 \times 15$  flow [14] as well as the triple-shock interaction where the  $15 \times 15$  interaction is modified by ramping the plate up by 10 degrees [30].

Since flow separation has important consequences on the performance of aerospace vehicles, it is natural to delve further by investigating the evolution of separation with interaction strength. This analysis can be greatly simplified and generalized within the framework of topology, specifically by reference to the appearance of critical points on the plate and within the flowfield. Such a study can emphasize the common features of separation in a wide range of flowfields.

At critical points, the velocity vector is undefined and, when they are observed in surface oil patterns, the shear stress vanishes. The two primary types of critical points are saddles and nodes/foci. Reference [25] contains a classification of the various types of critical points, their significance and the laws governing their behavior. Since numerous critical points are encountered, the following notation is adopted for clarity. On walls,  $S$  and  $N$  are utilized for saddles and nodes respectively. In off surface traces, the corresponding nota-

tion is  $s$  and  $n$ . Suffixes, superscripts or subscripts are employed to distinguish between critical points of the same kind. To simplify the application of relevant topological laws, “half” critical points are introduced as in [28] and denoted with primes (e.g.  $S'$ ,  $N'$ ). In surface streamline patterns, such points occur on lines of symmetry when only one side of the pattern is plotted. In symmetry-plane patterns, such “half” points occur at intersections with surfaces.

It is convenient to focus on symmetric flows, since the existence of a plane of symmetry provides a unique setting to differentiate the more complex set of phenomena accompanying 3D separation from those encountered in 2D. Consider the fully separated  $15 \times 15$  interaction at Mach 8. Computations with the Baldwin-Lomax model, reveal the surface pattern shown in Figure 5 (top) where the lines of coalescence/divergence are marked – they are the same as at Mach 4 and in good agreement with the experimental observation of [27]. An enlarged view of the region where the two PSs meet is presented in Figure 5(bottom). Four critical points, arranged in a diamond-shaped pattern, are easily identified. The two primary lines of coalescence come together at an attracting (or stable) node of separation NS — this is the only possibility if fluid is to locally approach the symmetry plane from upstream as well as from the sides. Two off-center-line saddle-points ( SP) are formed symmetrically on either side of the center-line. A repelling node of attachment NA is formed downstream. Precisely the same topological structure is observed in the Mach 4 computation of Figure 2.

The nature of the fully separated flow is further clarified by examining streamlines whose traces are restricted to the symmetry plane. Figure 6 depicts such particle paths (double-arrows) together with the previously discussed surface streamlines (single-arrows). The observation that the separating streamline on the symmetry plane does not reattach is consistent with the separated boundary layer surface depicted in Figure 4; in fact, such traces may be interpreted as intersections of stream surfaces with the symmetry plane. There is thus no closed 2D bubble in the computed flow. Rather, the region beneath the separating streamline is occupied by fluid arriving from the

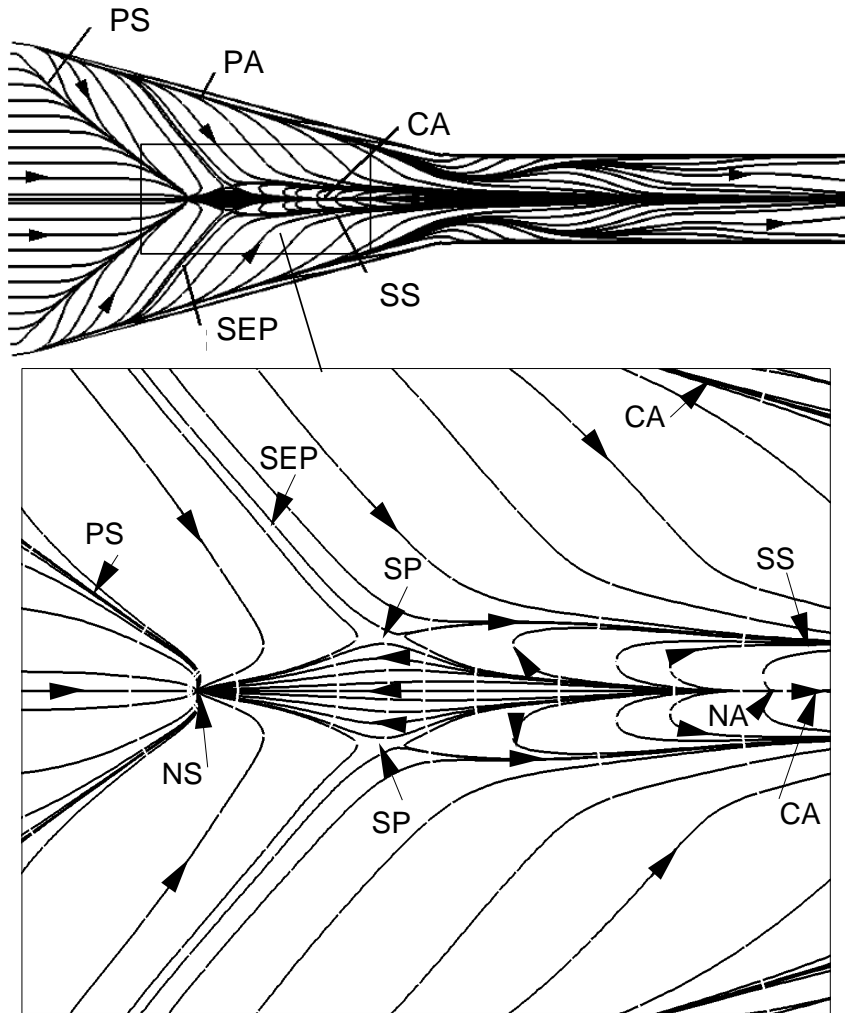


Figure 5: Surface pattern in Mach 8,  $15 \times 15$  interaction.

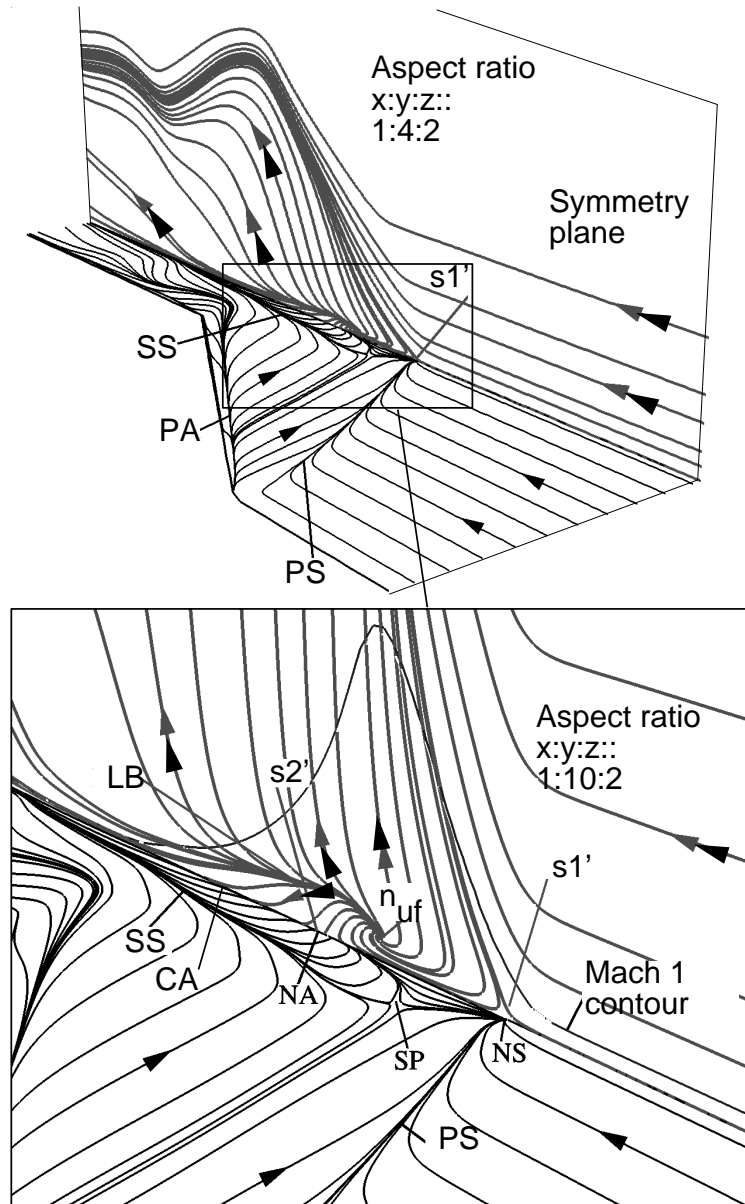


Figure 6: Streamlines on symmetry plane (double arrows) plotted with surface oil flow (single arrows), Mach 8,  $15 \times 15$  interaction.



span-wise direction. Figure 6 (bottom) shows details of the pattern in the vicinity of the critical points. The stable nodes, NS and NA on the plate are saddles of separation ( $s1'$ ) and attachment ( $s2'$ ), respectively, in the symmetry plane. In addition, another critical point occurs within the flow. This unstable focus,  $n_{uf}$ , is effectively an off-surface stagnation point which arises out of the vortex interaction regime.  $n_{uf}$  is located very near the plate, at  $0.02\delta \sim 0.7\text{mm}$ , and requires a highly clustered mesh in order to be observed. In this case, there are 13 mesh points between  $n_{uf}$  and the plate. Also noted in Figure 6 is a line of bifurcation (LB) emanating from  $n_{uf}$ . The flow beneath this line attaches at CA.

The various features observed in Figure 6 are formed gradually as the interaction strength is increased. Critical points appear in pairs to give rise to new bifurcations in the topological structure. The manner in which this process occurs has been gleaned from a large number of computations on symmetric  $7 \times 7$ ,  $11 \times 11$  and  $15 \times 15$  configurations at several Mach and Reynolds numbers and with many different turbulence models. The common features evolving from a detailed study of these computations are summarized in Figure 7, where again particular emphasis is placed on the region in the vicinity of the symmetry plane. Figure 7(a) depicts the schematic in the limit of complete absence of interaction, i.e., when the fin angles are both zero. In this case, both the surface and symmetry plane lines are undisturbed. Figure 7(b) shows the situation for the relatively mild  $7^\circ \times 7^\circ$  case. A distinct convergence of lines is evident in two regions, one along the ray of the primary line of coalescence PS and the other downstream and parallel to the symmetry plane, where the secondary separation line, SS, may be expected to form at stronger interactions. Symmetry plane traces indicate that fluid moves away from the plate under the influence of the adverse pressure gradient, but without formal separation.

With increasing interaction strength, Figure 7(c), PS is further strengthened in the sense that the asymptote is more sharply defined. As this line approaches the plane of symmetry, however, the degree of convergence is reduced as it turns parallel to the line of symme-

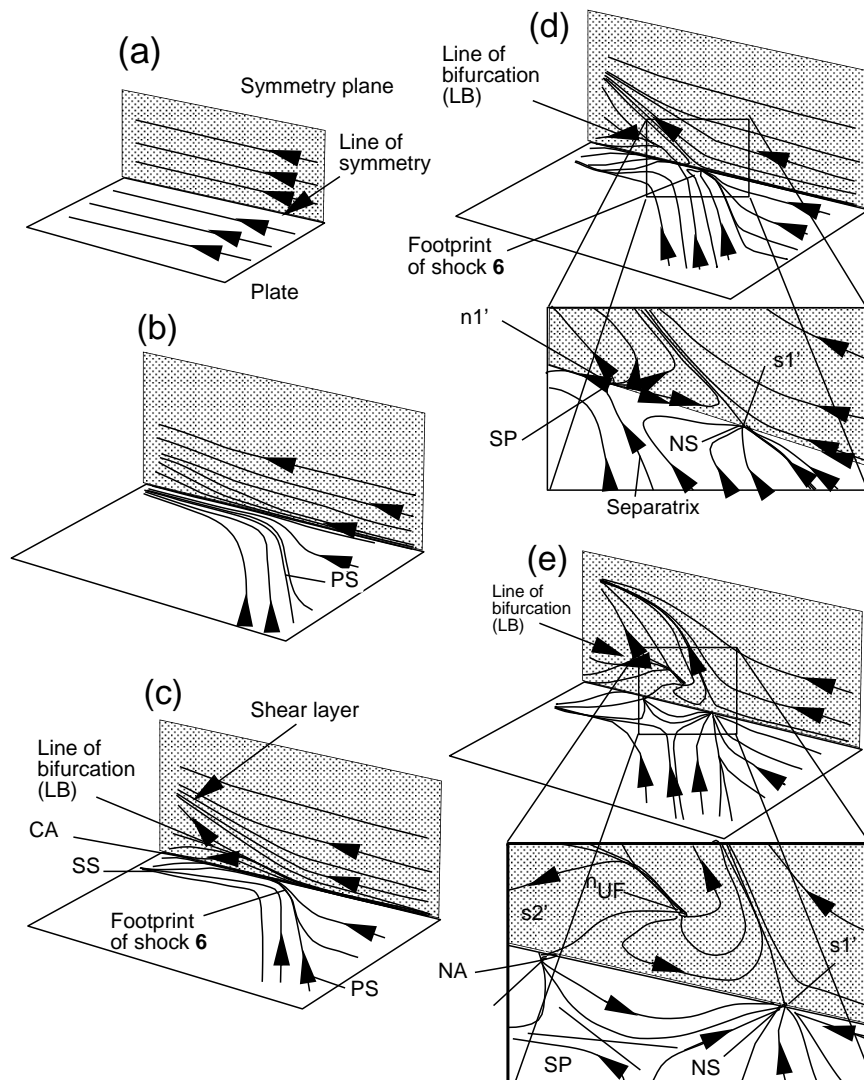


Figure 7: Observed evolution of the computed separation topology with increase in interaction strength.

try. All lines originating from upstream then approach the symmetry plane where they are squeezed in the narrow channel between PS and the line of symmetry. On the downstream side of PS, the degree of convergence (to PS) is relatively mild. Here each line is turned stream-wise under the influence of a shock, **6**, which is further discussed in a later section. These lines then form SS roughly parallel to the line of symmetry. On the symmetry plane, the incoming boundary layer is lifted from the plate to form a shear layer as marked. Beneath this layer forms a line of divergence/bifurcation, denoted LB, signifying the approach of fluid from the sides towards the symmetry plane. Figure 7(c) also affirms a basic distinction between 2D separation on the one hand and 3D separation on a symmetry plane on the other. Whereas the boundary layer has essentially separated from the surface, there is no reversed flow region.

Further increase in interaction strength produces the critical points shown in Figure 7(d). On the symmetry plane, an upstream saddle  $sl'$  and a downstream node  $nl'$  are observed, which correspond on the plate to the node NS and saddle SP, respectively. A region of reversed flow now exists. Thus, the skin-friction coefficient becomes negative for a short distance along the centerline. However, in contrast to the 2D situation, in which fluid separates at the first point of zero  $C_f$  and reattaches at the second, in 3D, separation occurs from both critical points. In the last frame, Figure 7(e), the downstream critical point bifurcates to yield the topological pattern of Figure 6 which has been discussed earlier.

### 3.2 Cylinder/offset-flare interaction

The construction of an off-surface flow model by utilizing surface oil flow patterns together with computations is now illustrated for the interaction caused by the cylinder-offset flare model shown earlier in Figure 1(bottom). The experimental data were obtained by Wideman et al. [6]. The problem is especially interesting since these data contain numerous critical points whose presence and locations can be used to assess this aspect of the calculations. For this reason, the numerical designation of the critical points closely follows the

experimental inference.

Figure 8 shows two views of the computed surface pattern, obtained with the  $k$ - $\epsilon$  model from  $\theta = 0$  degrees and  $\theta \sim 140$  degrees, where  $\theta$  is measured from the vertical as shown in Figure 1. A saddle-node combination, S1-N1, is observed near the juncture on the upper symmetry plane. Two saddles, denoted S4' and S5', are formed on the lower plane of symmetry. Note that since the structure on only one side of the line of symmetry is plotted ( $\theta \leq 180$  deg), these are marked as half critical points. The computed results show two additional critical points: node N2 and its mirror image on the other side of the symmetry plane, N4 (not shown). While N1 is a repelling or unstable node, i.e. fluid in its vicinity moves away from it, N2 and N4 are attracting or stable nodes.

On the upper portion, Figure 8(top), the incoming fluid forms a line of coalescence, LC1, upstream of the juncture. This line originates on one separatrix of S1 and terminates at N2 (Figure 8(bottom)). The convergence of lines is very tight in the vicinity of the two critical points but less so in the intermediate region,  $40 < \theta < 100$  degrees. A second line of coalescence LC2 forms on the separatrix emanating from S4' and also terminates at node N2. Thus, the fluid separates in a 3D fashion around the entire periphery of the cylinder. A line of divergence, LD, originates at N1 and can be clearly observed for short distances away from it but gradually becomes less distinct with increasing  $\theta$ . For this non-axisymmetric 3D situation, subsequent analysis will demonstrate that attachment is not feasible in a *continuous* fashion along the entire periphery of the flare. One of the lines emanating from node N1 forms a separatrix for S5' and is marked *Sep* in Figure 8(bottom).

All the topological information in Figure 8 can be presented in a single figure by “unwrapping” the surface with a suitable transformation. This tactic does not alter the topological structure and greatly facilitates comparison with experimental data. Such an exercise, results of which are presented in Figure 9, demonstrates the clear similarity between experimental and computed patterns. Points of agreement include the presence of S1, N1, S4, S5, and N2 (and its

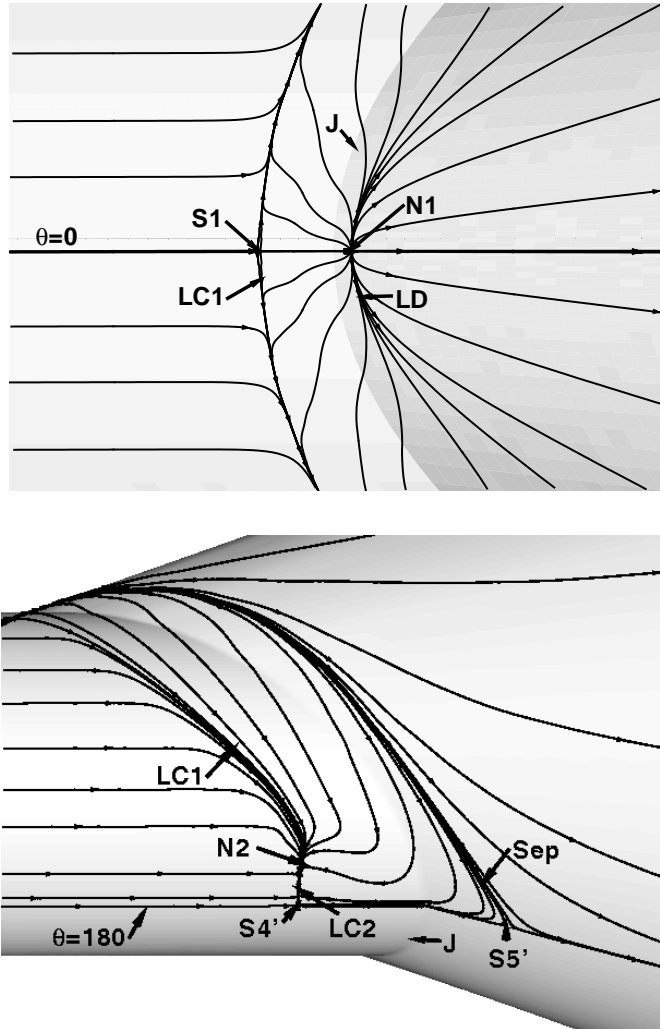


Figure 8: Surface streamline structure obtained with the  $k-\epsilon$  method on M1, J=Juncture: (a) view from  $\theta = 0^\circ$ ; (b) view from  $\theta \sim 140^\circ$ .

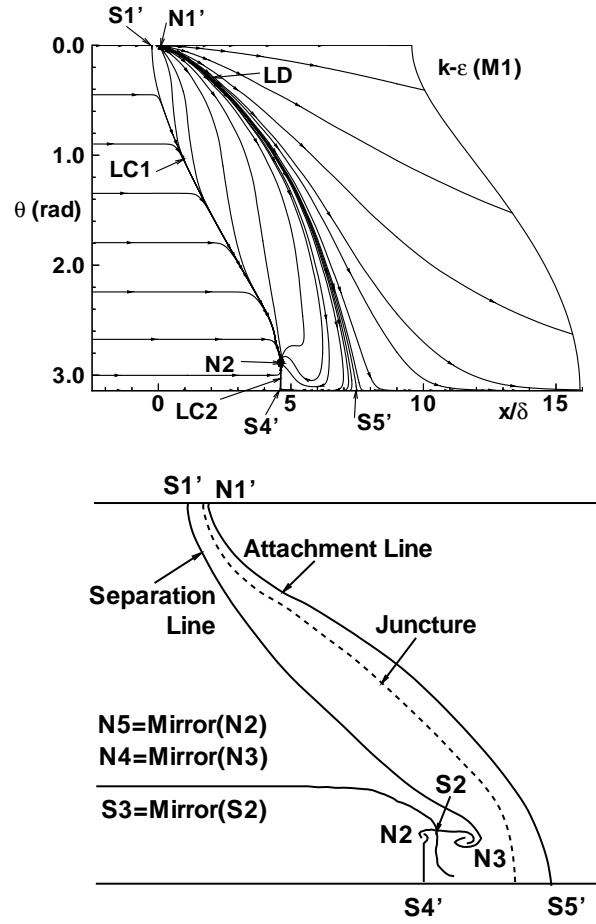


Figure 9: Unwrapped surface streamline structure. Top:  $k-\epsilon$  computation; bottom: re-sketched experimental inference from [6]. Not to scale.

mirror image on the other side of the vertical plane of symmetry, N5, not shown). Similarly, the lines LC1, LC2, and LD are also common to experiment and computation. The main discrepancy arises in the vicinity of node N2, where the experimentalists note some uncertainty in results from various runs [6]. Additional computations [11] confirm that enriched spatial discretization in this area does not alter the computed topology. Although this aspect of the comparison clearly deserves additional work, for the present it is assumed that the computed structure is a “kinematic truncation” [28] of the experimental observation. As noted in [25, 28], isolated critical points occurring closely together take on the character of a simpler configuration if viewed on a large scale. Thus, the computed node N2 exhibits some of the features associated with the N2-S2-N3 complex identified in experiment. In this regard, the notation N2 employed for the single computed node is not to be construed as a closer identification with experimental N2 but rather as representative of the experimental N2-S2-S3 trio. Another interesting aspect observed in Figure 9 is the direct connection of two saddle-points,  $S'_4$  and  $S'_5$ . Such connections are known to be structurally unstable [26], but can exist in cases of “strong symmetry” [25]. With the Baldwin-Lomax model, the downstream saddle  $S'_5$  bifurcates into an off-symmetry plane saddle and is replaced by a node on the symmetry plane. The effect of this variation on the overall flowfield is minor and the pattern of Figure 9 may be considered a kinematic truncation in this regard also.

The description of the flowfield in terms of its vortical structures can again be accomplished by judiciously releasing particles so that their trajectories approach the vicinity of the above topological features. For example, the flow structure in the vicinity of the upper plane of symmetry is displayed in Figure 10. Again, it is illuminating to apply an artificial aspect ratio to highlight each regime. Some features of the surface topology are marked to display their relationship to the off-surface structure. The “upper” surface of separation shown emanating from LC1 rolls upward and span-wise to form a vortical structure under the influence of the adverse pressure gradi-

ent associated with the flare-induced shock wave. The outer surface, only a sliver of which is shown, is constituted of fluid attaching at LD. It is immediately apparent that this surface of attachment cannot exist smoothly around the periphery, as may happen for example in an ideally axi-symmetric situation. In this 3D case, a kinematically infeasible situation would result where the fluid in the incoming boundary layer beneath is trapped.

Proceeding in the above manner, dividing surfaces can be constructed and supplemented with particle traces released in the vicinity of the critical points. The emerging description of the flow is summarized in Figure 11. Briefly, the boundary layer on the cylinder separates around the entire periphery upstream of the juncture. A horseshoe type of vortical structure is formed near the upper symmetry plane as is typical of situations where an obstacle is placed in an oncoming fluid (juncture flows). The legs of this vortex wrap around the juncture and turn stream-wise near the lower symmetry plane. Fluid entrained into the vortical field near the upper symmetry plane is vented downstream near the lower symmetry plane. This results in a dual scroll-like stream surface straddling the lower symmetry plane.

As noted earlier, the number and types of critical points possible are related through a set of topological laws (see for example [26]) which relate the number of nodes/foci to the number of saddles. It is a relatively simple matter to confirm that these laws are upheld. In the above cases, local balance requires equality between the number of nodes and saddles. By counting the primed critical points as “half” points, it is clear that each of the above patterns for both configurations satisfies this law precisely. It was noted earlier that a topological description greatly facilitates the detection of common features of 3D separation in vastly differing situations. In fact, several of the substructures detected in the present work have been previously derived through a mathematical analysis of the Navier–Stokes equations (see, for example, [31]) in situations not restricted to STBLI. The flows past several other configurations have also yielded similar topological structures [32].

Before concluding this discussion of the cylinder/offset flare flow,



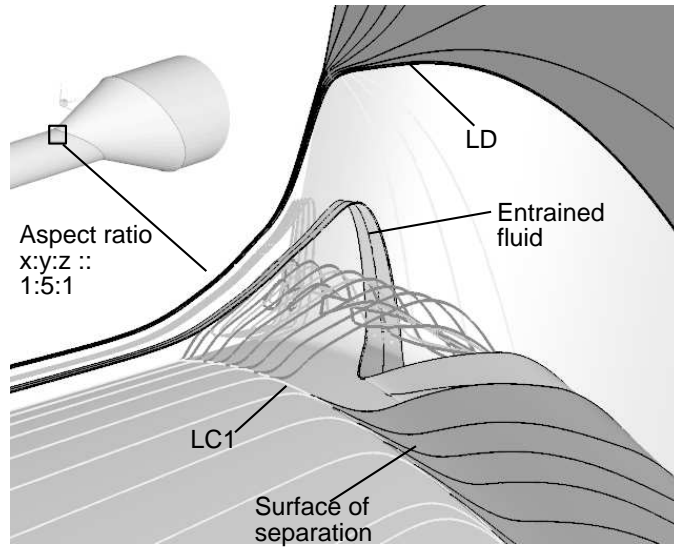


Figure 10: Flow structure in vicinity of upper plane.

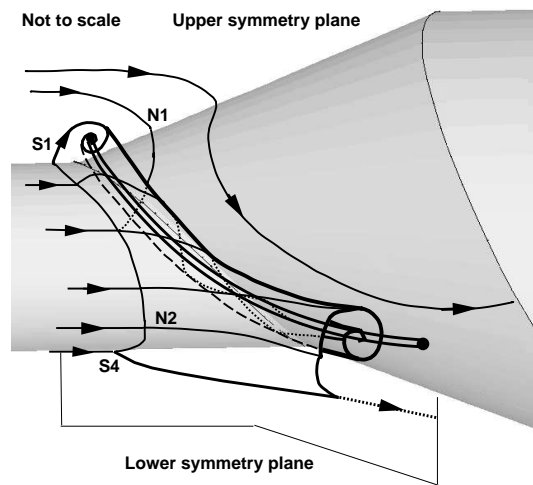


Figure 11: Schematic of computed cylinder/offset-flare flowfield.

it is noted that extensive comparisons of computational results with several turbulence models and experimental data may be found in [10]. Quantities examined include locations of critical points, upstream influence of the flare, surface pressures and skin-friction coefficients. The overall agreement can again be characterized as very good for all quantities with the exception of skin-friction coefficients which are sensitive to the turbulence model employed. Further comment on this aspect of computational fidelity is deferred to Section 5.

## 4 Flowfield dynamics

The above description has been based exclusively on the velocity field and may be termed as the kinematic structure. A practical flowfield model must, at the minimum, correlate this description to the complex pressure and density fields that form an integral part of the dynamics. This section explores the manner in which computations can yield such a unified understanding. These fields also provide a context in which to evaluate the quantitative accuracy of the computationally deduced flow structure by direct comparison with experimental data in regions away from the surfaces. Attention is restricted to the double-fin, since this is the more extensively examined flowfield.

Mean quantitative field measurements consist primarily of pitot pressure and yaw angle data on cross-flow planes. For the Mach 4  $15 \times 15$  interaction, Figure 12 shows computed and measured [33] pitot pressures on a cross-flow plane located  $32\delta$  downstream of the fin leading edge. Note that the experimental data do not extend to the surfaces. The computational result was obtained with the  $k-\epsilon$  model coupled with the Beam-Warming scheme. The second- and fourth-order artificial dissipation added for stability is manifested in the smearing of the shock wave in the inviscid regions. Nonetheless, the features of the interaction are accurately reproduced. The dominant structure in both experiment and computation is an inverted heart-shaped low pitot pressure core near the center of the channel.

It is fairly straightforward to correlate this cross-flow map to the streamline structure elucidated earlier. The shape of the low

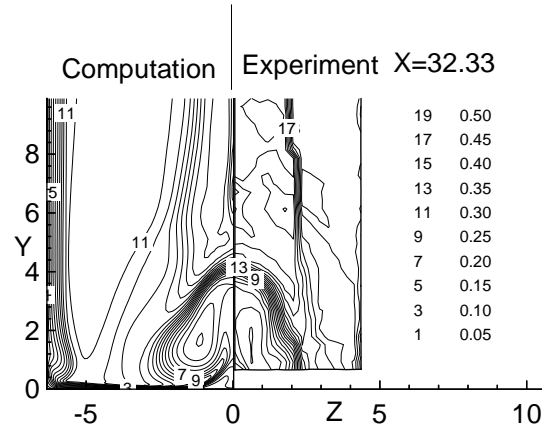


Figure 12: Comparison of pitot pressure with  $k-\epsilon$  model on  $X = 32.33$  plane with experiment, Mach 4,  $15 \times 15$  interaction.

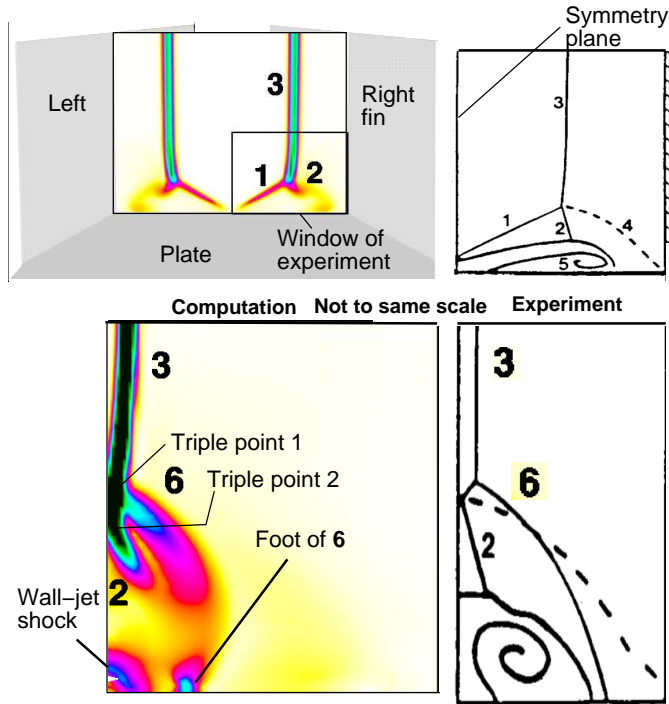


Figure 13: Shock structure comparison at two locations in Mach 4,  $15 \times 15$  interaction. Left: computed  $|\vec{\nabla}p|$ ; right: experimental sketch [4], reproduced with permission.

pitot pressure region corresponds closely with the arch-like profile of the separated boundary layer surface (Figure 4 (top)). It is easy to confirm that the outer periphery is formed by the lifting of the incoming boundary layer together with fluid in the vortex interaction regime, which as noted earlier, forms a shear layer with the separated boundary layer. The entrainment regime brings high energy fluid from the upstream far field to regions very close to the plate, thus encircling the core.

In addition to pitot pressure, the shock structure is also of great significance in the performance of inlets. Because of its complicated three-dimensionality, the shock structure is typically visualized through its trace on successive cross-flow planes. Garrison et al. [4] have published extensive planar laser scattering (PLS) experimental data on the Mach 4  $15 \times 15$  interaction. The computed shock structure can be obtained by plotting the magnitude of the pressure gradient ( $|\vec{\nabla}p|$ ), which is found to be far more suitable for ease of shock-detection than static pressure. Since upwind schemes are known to have superior shock-capturing characteristics, the following description is based on computations with the upwind-biased Roe flux-difference split scheme.

Figure 13(top) shows the trace of the shock just downstream of the two fin leading edges for the Mach 4,  $15 \times 15$  case. Two  $\lambda$  shocks are evident, comprised of the separation, rear and inviscid shocks (designated **1**, **2**, and **3**, respectively) similar to that observed in single-fin interactions [34]. The experimental sketch spans a window of the channel on one side of the symmetry plane as shown. It also includes a slip surface **4** and a separated region **5**. Neither is observed in the pressure field but both are clearly observed in the density field (not shown). As this cross-flow cutting plane is moved downstream, the traces of these two “primary”  $\lambda$ s appear to cross each other, resulting in a pair of distorted but connected “secondary”  $\lambda$  systems as described in detail in [4, 9]. In this process, several extremely complicated patterns may be observed on cross-flow planes. One such is shown in Figure 13 (bottom). Two distinct but very closely located triple points are visible. Shock **6** is the separation shock associated

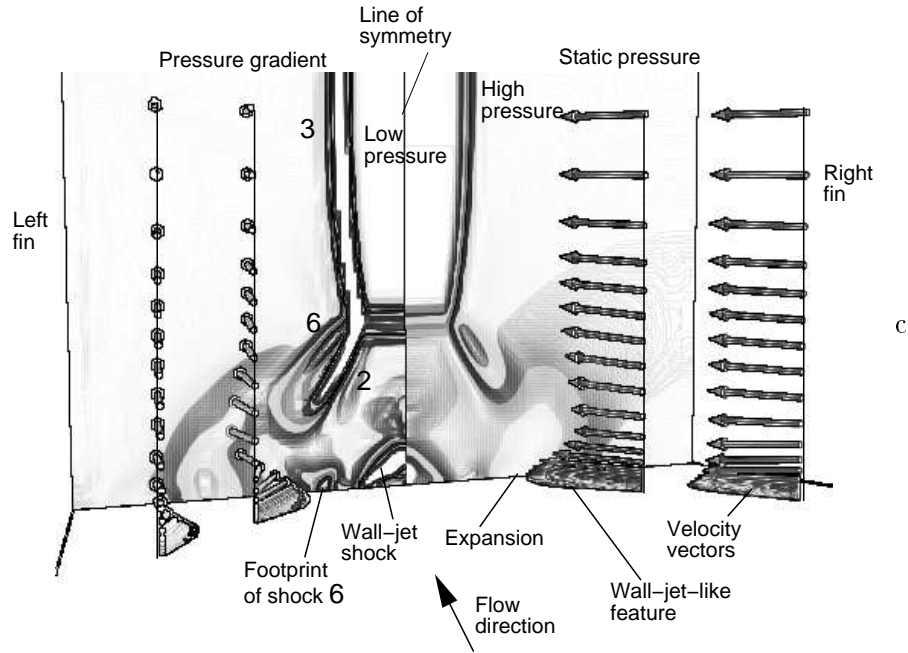


Figure 14: Correlation between shock and streamline structure: interaction of wall-jet and shock structures.

with the left fin  $\lambda$  system which has crossed the symmetry plane. A wall-jet shock forms in the center of the channel and is discussed further below.

To illustrate the manner in which the shock and streamline structures may be correlated, Figure 14 depicts the pressure gradient (left) and static pressure (right) on either side of the line of symmetry in a cross-flow plane. A select set of 3D velocity vectors is superposed. A careful examination of Figures 14, 4(top) and 13 reveals that fluid in the entrainment regime first encounters the inviscid shock, **3**. This compressed fluid then experiences a favorable pressure gradient, first downward toward the plate, and then span-wise toward the symmetry plane (Figure 14). This is accompanied by an increase in velocity

magnitude, and a wall-jet-like feature is formed. This fluid then encounters two distinct adverse pressure gradients, the first associated with the shock wave **6** which tends to turn the fluid in the stream-wise direction. The degree of turning is insufficient to align the fluid velocity in the downstream direction. The two wall-jet-like structures then impinge on each other. Due to continuity constraints, the fluid velocity component in the span-wise direction must vanish at the symmetry plane. This stagnation-like process is accomplished by the wall-jet shock (Figure 14), which creates a local high-pressure region also observed in experimental data [4]. The adverse span-wise pressure gradient so established causes separation of the near-plate flow at the line of coalescence, SS.

The availability of a computed field permits the examination of a nearly endless set of combinations of variables. Some of the more illustrative of these are discussed in [9, 12] and include helicity density and the quantity  $\vec{V} \cdot \vec{\nabla} p$  which is useful in distinguishing expansions from weak compressions. Another interesting quantity is vorticity, which plays an extremely important role in separated flows (see [35] for an illuminating discussion). Although the vorticity dynamics of compressible turbulent interactions is rather complicated, even a simple description of the computed vorticity field highlights aspects not readily apparent in other variables. Such an effort has been presented in [12] for symmetric as well as asymmetric cases. In the former, the cross-flow structure appears mushroom-like with a cap formed by the separated boundary layer and a stem formed by separation of the entrained regime at SS. On the other hand, in asymmetric cases, the vorticity field displays two distinct regions, an inner vortical core and an outer annulus. The two regions are comprised of incoming boundary layer fluid processed through the strong and weak shock waves, respectively.

## 5 Comments on turbulence modeling

Before concluding, the above understanding of the flowfield is utilized to comment on some aspects of the quantitative comparison of com-

puted data with experiment. In addition to pitot pressure and shock structure, surface pressures on the plate are also computed accurately. This is illustrated in Figure 15, which shows surface pressure along the three cross-flow stations, I, II, and III in Figure 3(bottom). At the first two stations, the computational data lie within the experimental error band. At Station III, a small span-wise shift is evident in the two pressure distributions, but the agreement may be termed reasonable nonetheless for practical purposes. Surface pressures along the centerline of the channel for the  $7 \times 11$ ,  $7 \times 15$  and  $11 \times 15$  interactions as presented in [12] also show excellent agreement with experimental data.

As noted earlier, computations show large discrepancies in gradient-related quantities, such as skin-friction coefficients and heat-transfer rates. This failure may be attributed to a combination of several factors. One reason is poor local mesh resolution in regions of extremely high gradients, such as near lines of separation and attachment. A related effect is that a small “mismatch” between computation and experiment, say in fin angle or in channel width, can induce a shift of salient features. In regions of rapid variation, this effect can manifest as misleadingly large errors in the comparison of pointwise quantities. However, the dominant cause of inaccuracy is the turbulence model itself. The previous discussions have clearly highlighted the three-dimensionality of the flow, particularly in the vicinity of secondary structures and where shock-induced separation occurs. These flows are characterized by large pressure gradients, streamline curvature and anisotropy. High expectations from eddy viscosity models, particularly those based on 2D experience, are thus perhaps unrealistic.

These points are illustrated by considering  $C_f$  predictions in the Mach 4,  $15 \times 15$  interaction. Figure 16 displays span-wise ( $z/\delta$ ) variation of the skin-friction coefficient in a  $15 \times 15$  interaction with two different turbulence models. The experimental measurements at  $x/\delta = 25.3$ , obtained by Garrison et al. [5], are plotted with computational predictions of the baseline model. The data are in good agreement in  $4 < z/\delta < 8$  but show large quantitative discrepancies near the symmetry plane,  $z/\delta < 4$ . More significantly, even the trends

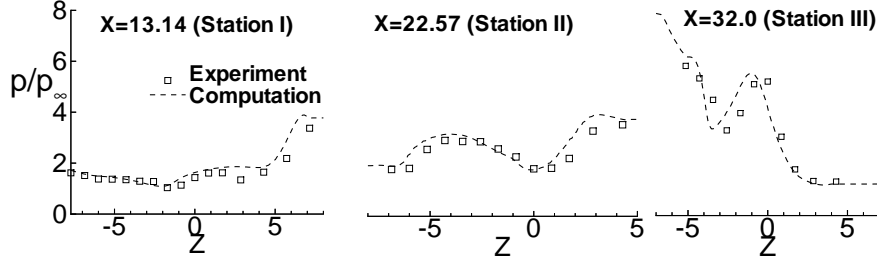


Figure 15: Comparison of surface pressure on cross-flow stations for  $7 \times 15$  case.  $X = x/\delta$ . Experiment of Zheltovodov et al. [8].

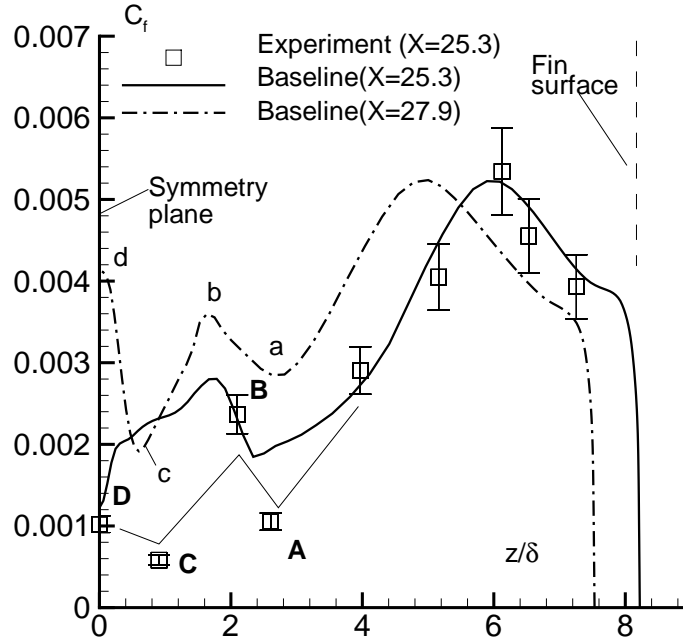


Figure 16: Skin-friction coefficient on plate along span-wise line at stream-wise location  $X = x/\delta = 25.3$ . Experiments of Garrison et al. [5].



in this latter region are inaccurate since the “W” feature (A-B-C-D) observed in experimental  $C_f$  values is completely absent. Although the measurements are sparse in this region, the experimentalists note that these trends cannot be attributed to data scatter since they are confirmed by oil fringe distributions [5]. Given that all of the surface oil flow features are reproduced in the computation (Figure 2), this is initially a surprising observation.

An explanation for this anomaly can be obtained by combining an understanding of the flowfield with further probing of the computed flow. The last curve of Figure 16 shows  $C_f$  values at  $X = 27.9$  with the baseline model. This location, roughly  $2.5\delta$  downstream of the experimental observation, reveals the same “W” profile. An explanation for these undulations can be proposed by integrating the information presented in Figures 4 and 14. As noted earlier, a wall-jet-like structure results when the entrained fluid encounters a favorable pressure gradient in its path from the corner to the symmetry plane. This is accompanied by a decline in  $C_f$  values in the range  $4 < Z < 8$ . The wall-jet-like feature displays relatively little stream-wise velocity as noted in the velocity vectors of Figure 14. Since there is also only modest stream-wise variation of this feature – note the similarity of the  $C_f$  profiles at  $X = 25.3$  and  $X = 25.9$  in the region  $Z > 4$  – the sequence of processes encountered by a typical streamline can be correlated to a large extent with the cross-flow plane data. The wall-jet first encounters an adverse pressure gradient due to the foot of shock **6**. This interaction is insufficient to cause separation but results in an initial decline in  $C_f$  (point *a* in Figure 16) followed by strong recovery to reach a maximum at point *b*. These trends are consistent with those experienced by a boundary layer under the influence of a rapid pressure gradient, but which is inadequate to cause separation [36]. The jet subsequently impinges on the symmetry plane at an oblique angle in a stagnation-like process causing a second pressure rise associated with the wall-jet shock. This causes a second decline in  $C_f$  and ultimately induces separation associated with SS. Near the centerline, the flow is highly three-dimensional due to the presence of the secondary vortices and the local behavior of

the  $C_f$  profile is strongly dependent upon features outside the cross-flow plane under study. Thus, the location of secondary separation does not coincide with the local minimum,  $C$ , in this cross-sectional plane. However, the center-line is itself a line of attachment (CA) and exhibits a local  $C_f$  (Figure 16) maximum. Thus, discrepancies in trends are partly associated with the displaced development of coherent features in experiment and computations.

It was stated in Section 2 that both the oil-flow pattern on the plate as well as the shock structure were found to be relatively insensitive of the turbulence model and in good agreement with the experiment. Relatively little comment has been made so far on the flowfield in the vicinity of the fins. In symmetric cases, the flow here is relatively benign and consists of a developing boundary layer (see, for example, Figure 12) interacting with the shock-wave from the opposite fin only at locations downstream of the region examined. This is not the case, however, in the highly asymmetric  $7 \times 15$  case. As depicted in Figure 4(bottom), the 7 degree sidewall is subjected to impingement of the vortical structure. This interaction is sensitive to the turbulence model. However, it is now examined further to illustrate the point that even when the details of a particular aspect of the interaction are dependent upon the turbulence model, computations can still be utilized to develop an understanding of the flow structure for engineering purposes.

The sidewall surface patterns obtained by experiment [8] are displayed in Figure 17(top). The corresponding prediction with the baseline  $k-\epsilon$  model is shown in Figure 17(middle). The notation for various topological features again follows that of the experimental inference. Although the separation and attachment lines,  $S_5$  and  $R_5$ , respectively, are observed in both patterns, significant discrepancies are evident in the size of the reversed flow region. More importantly, the prominent focus denoted  $F_1$  is absent in the computations. A possible cause of this disagreement is based on the state of the fin boundary layer. In the baseline model, the fin boundary layer becomes turbulent forthwith at the fin leading edge, a situation which may not mirror the actual situation in the experiment where transi-

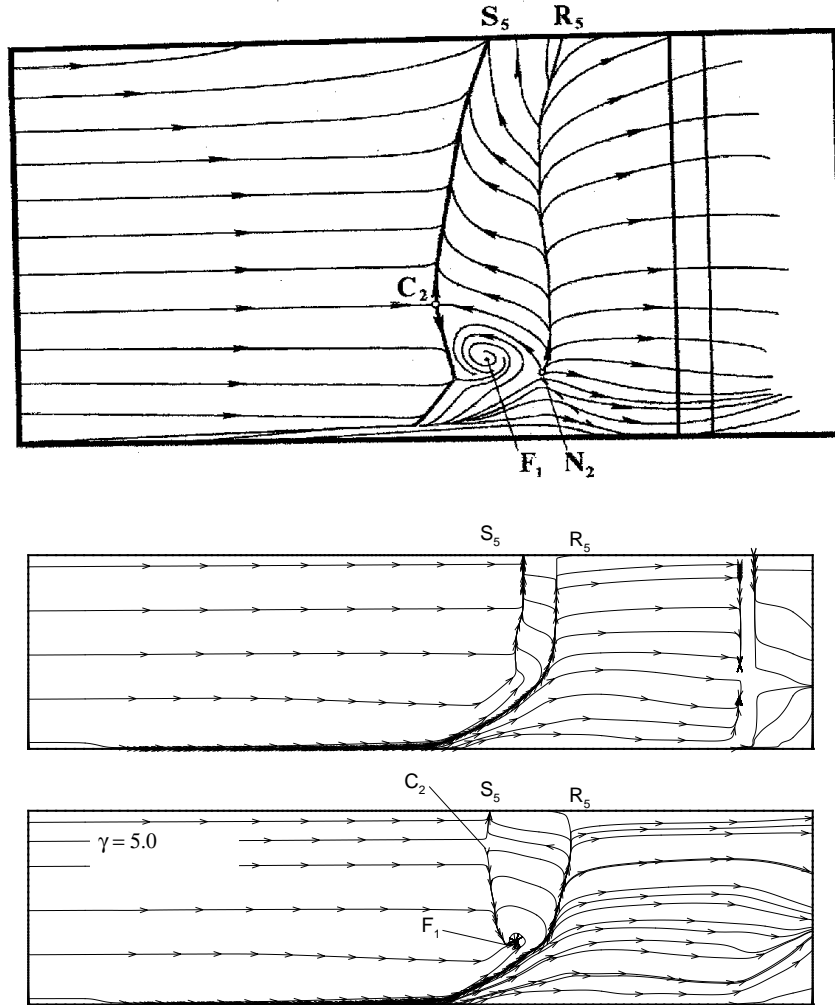


Figure 17: Comparison of experimental inference of Zheltovodov et al. for sidewall surface pattern on 7 deg fin of  $7 \times 15$  interaction. Top: experiment, reproduced with permission. Middle: baseline  $k-\epsilon$  model. Bottom:  $k-\epsilon$  model with limiting of turbulence energy production. C=saddle-point, F=Focus, S=Separation, R=Attachment.

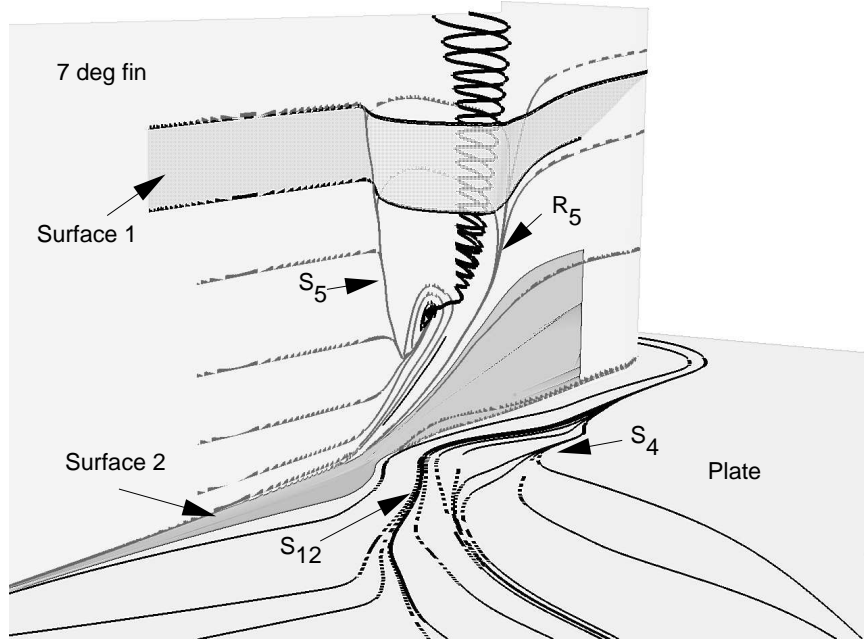


Figure 18: Flowfield structure caused by vortex/sidewall interaction in  $7 \times 15$  case.

tion may occur some distance downstream.

An elegant technique to restrain transition of a turbulent boundary layer is to limit the production of turbulent kinetic energy [37]. The impact of this modification on the sidewall surface pattern is shown in the bottom frame of Figure 17. The improvement in the comparison with experimental data is tangible: note particularly the increased reversed flow region between  $S_5$  and  $R_5$  and the appearance of the focus-saddle combination,  $F_1-C_2$ , which satisfies the local rules of topological bifurcation.

Having reproduced the experimental result, the flowfield resulting from the sidewall-vortex interaction can now be elucidated. As shown in Figure 18, the fin boundary layer separates at  $S_5$ , and does not

reattach to the fin. Rather, the fluid attaching at  $R_5$  originates near the fin/plate corner. A truncated version of this regime is depicted as Surface 2. The significance of the focus is also clearly evident from Figure 18: this represents the lift-off of the corner vortex which then traverses vertically parallel to the fin rather than downstream. The interaction can be expected to evolve into the common quasi-two-dimensional situation at distances far from the fin/plate corner.

## 6 Conclusion

Numerical solutions of the full Reynolds-averaged compressible Navier–Stokes equations in mass-averaged variables describe the dominant primary and secondary features of 3D STBLI. The wealth of data obtained has been carefully processed to develop simple but broad flowfield models for the double-fin and cylinder/offset flare interactions. Such an understanding can not only aid practical analysis of these flows, but also provide guidance in turbulence model choice and development.

Since the overall flow is predominantly rotational and inviscid away from the close vicinity of the surface, engineering accuracy is assured by choosing a high-resolution shock-capturing method together with popular turbulence models which can accurately reproduce the properties of the incoming boundary layer. The major discrepancies associated with skin-friction and heat transfer coefficients are strongly dependent upon the properties of the post-attachment or “freshly” attached flow in the entrainment regime. These mechanisms are complex and pose a major challenge. Some discrepancies in the comparison of pointwise quantities are associated with displaced development of features, particularly where gradients are large.

Several areas of future research may be identified. From an engineering standpoint, a proper calibration of turbulence model, eddy viscosity-based or higher-order may be feasible for a wide range of flow parameters. Such calibration must however be performed in 3D and is a computationally intensive endeavor. The dynamics of compressible turbulence remain an issue of present research and can

be addressed through direct and large-eddy simulations. However, the success of this approach for STBLI awaits further progress in numerical algorithms, physical modeling and computational technology. These advances will however facilitate an examination of inherent STBLI unsteadiness, which is an area of great engineering and scientific importance.

## Acknowledgements

The work described above has benefited from extensive collaboration with and support of J.S Shang and M.R. Visbal. The author also acknowledges several interactions with M. J. Aftosmis, J. R. Edwards, T.J. Garrison, A.I. Maksimov, J. Poggie and A.A. Zheltovodov. The work has been supported by the Air Force Office of Scientific Research under several grants monitored by Drs. M. Jacobs, R. Canfield, L. Sakell, and S. Walker. Computational resources were provided by the Major Shared Resource Centers at CEWES, NAVOCEANO, and ASC and by the Numerical Aerodynamic Simulation (NAS) facility.

## References

- [1] Settles, G.S., and Dolling, D.S., Swept shock wave/boundary-layer interactions, In *Tactical Missile Aerodynamics: General Topics*, ed. M.J. Hemsch, Vol. I, American Institute of Aeronautics and Astronautics, 1997.
- [2] Panaras, A.G., Review of the physics of swept-shock/boundary layer interactions, *Prog. Aerospace Sci.*, **31**, pp. 173–244, 1995.
- [3] Zheltovodov, A.A., Maksimov, A.I. and Shulein, E.K., Development of turbulent separated flows in the vicinity of swept shock waves (Translated from Russian), In *The Interactions of Complex 3-D Flows*, ed. A.M. Kharitonov, Institute of Theoretical and Applied Mechanics, Novosibirsk, pp. 67–91, 1987.

- [4] Garrison, T.J. and Settles, G.S., Interaction strength and model geometry effects on the structure of crossing-shock wave/turbulent boundary-layer interactions, *AIAA Paper 93-0780*, 1993.
- [5] Garrison, T.J. and Settles, G.S., Laser interferometer skin-friction measurements of crossing-shock wave/turbulent boundary-layer interactions, *AIAA Paper 93-3072*, 1993.
- [6] Wideman, J.K., Brown, J.L., Miles, J.B. and Ozcan, O., Surface documentation of a 3-D supersonic, shock-wave/boundary-layer interaction, Technical Report, NASA TM 108824, NASA Ames Research Center, California, 1994.
- [7] Kussoy, M.I. and Horstman, K.C., Intersecting shock-wave/turbulent boundary layer interactions at Mach 8.3, Technical Report, NASA-TM 103909, NASA Ames Research Center, California, 1992.
- [8] Zheltovodov, A.A. and Maksimov, A.I., Symmetric and asymmetric crossing-shock-waves/turbulent boundary layer interactions, Final Report, EOARD contract F61708-97-W0136, ITAM, Russian Academy of Sciences, Novosibirsk, Russia, 1998.
- [9] Gaitonde, D.V. and Shang, J.S., The structure of a double-fin turbulent interaction at Mach 4, *AIAA Journal*, 33, (12), pp. 2250–2258, 1995.
- [10] Gaitonde, D.V., Edwards, J.R. and Shang, J.S., Performance of eddy-viscosity based turbulence models in a 3-D turbulent interaction, *AIAA Journal*, 34, (4), pp. 1590–1592, 1996.
- [11] Gaitonde, D.V., Shang, J.S. and Edwards, J.R., Structure of a supersonic three-dimensional cylinder/offset-flare turbulent interaction, *Journal of Spacecraft and Rockets*, 34, (3), pp. 294–302, 1997.
- [12] Gaitonde, D.V., Shang, J.S., Garrison, T.J., Zheltovodov, A.A., and Maksimov, A.I., Evolution of the separated flowfield in a

3-D shock wave/turbulent boundary layer interaction, *AIAA Paper 97-1837*, June 1997.

- [13] Dolling, D.S., Problems in the validation of CFD codes through comparison with experiment, In *AGARD Symposium on Theoretical and Experimental Methods in Hypersonic Flows*, Turin, Italy, 1992.
- [14] Gaitonde, D.V., Shang, J.S., and Visbal, M.R., Structure of a double-fin turbulent interaction at high speed, *AIAA Journal*, 33, (2), pp. 193–200, 1995.
- [15] Panaras, A.G., Algebraic turbulence modelling for swept shock-wave/turbulent boundary-layer interactions, *AIAA Journal*, 35, (3), pp. 456–463, 1997.
- [16] Knight, D.D. and Degrez, G., Shock wave boundary layer interactions in high Mach number flows – a critical survey of current CFD prediction capabilities, Technical report, AGARD AR-319, 1997.
- [17] Bradshaw, P., Progress in turbulence research, *AIAA Paper 90-1480*, June 1990.
- [18] Rubesin, M. and Rose, W., The turbulent mean-flow, Reynolds-stress and heat-flux equations in mass averaged dependent variables, Technical Report, NASA TMX-62248, 1973.
- [19] Baldwin, B.S. and Lomax, H., Thin layer approximation and algebraic model for separated turbulent flows, *AIAA Paper 78-0257*, January 1978.
- [20] Launder, B.E. and Sharma, B.I., Application of the energy dissipation model of turbulence to the calculation of flows near a spinning disk, *Letters in Heat and Mass Transfer*, 1, pp. 131–138, 1974.
- [21] Baldwin, B.S. and Barth, T.J., A one-equation turbulence transport model for high Reynolds number wall-bounded flows, *AIAA Paper 91-0610*, January 1991.



- [22] Spalart, P.R. and Allmaras, S.R., A one-equation turbulence model for aerodynamic flows, *AIAA Paper 92-0439*, January 1992.
- [23] Gaitonde, D.V., Edwards, J.R. and Shang, J.S., The computed structure of a 3-D turbulent interaction caused by a cylinder/offset flare juncture, *AIAA Paper 95-0230*, 1995.
- [24] Rizzetta, D.P., Numerical simulation of turbulent cylinder juncture flowfields, *AIAA Journal*, 32, (6), pp. 1113-1120, 1994.
- [25] Chapman, G.T. and Yates, L.A., Topology of flow separation on three-dimensional bodies, *Applied Mechanics Reviews*, 44, (7), pp. 329-345, 1991.
- [26] Tobak, M. and Peake, D.J., Topology of three-dimensional separated flows, *Annual Review of Fluid Mechanics*, 14, pp. 61-85, 1982.
- [27] Kussoy, M.I., Horstman, K.C. and Horstman, C.C., Hypersonic crossing shock-wave/turbulent-boundary-layer interactions, *AIAA Journal*, 31, (12), pp. 2197-2203, 1993.
- [28] Hunt, J.C.R., Abell, C.J., Peterka, J.A. and Woo, H., Kinematical studies of the flows around free or surface-mounted obstacles; applying topology to flow visualization, *Journal of Fluid Mechanics*, 86, (1), pp. 179-200, 1978.
- [29] Visbal, M.R., Structure of laminar juncture flows, *AIAA Journal*, 29, (8), pp. 1273-1282, 1991.
- [30] Gaitonde, D.V. and Shang, J.S., On 3-D shock-wave/turbulent boundary layer interactions at Mach 4, *AIAA Paper 96-0043*, January 1996.
- [31] Dallmann, U., Three-dimensional vortex structures and vorticity topology, *Fluid Dynamics Research*, 3, pp. 183-189, 1988.
- [32] Dallmann, U., Topological structures of three-dimensional flow separations, *DFVLR Report, 221-82 A 07*, Germany, 1983.

- [33] Settles, G.S. and Dodson, L.J., Hypersonic shock/boundary-layer interaction database: new and corrected data, Technical Report, NASA-CR 177638, 1994.
- [34] Alvi F.S. and Settles, G.S., Physical model of the swept shock wave/boundary-layer interaction flowfield, *AIAA Journal*, 30, (9), pp. 2252–2258, 1992.
- [35] Lighthill, M.J., *Attachment and separation in 3D flow*, ed. L. Rosenhead, Oxford UP, Oxford, UK, pp. 72-82, 1963.
- [36] Smits, A.J. and Muck, K-C., Experimental study of three shock wave/turbulent boundary layer interactions, *Journal of Fluid Mechanics*, 182, pp. 291–314, 1987.
- [37] Menter, F.R., Zonal two equation  $k - \omega$  turbulence models for aerodynamic flows, *AIAA Paper 93-2906*, July 1993.